Acta Biomaterialia xxx (xxxx) xxx

Contents lists available at ScienceDirect

Acta Biomaterialia

journal homepage: www.elsevier.com/locate/actbio

Full length article

Simultaneous tensile and shear measurement of the human cornea *in vivo* using S0- and A0-wave optical coherence elastography

Guo-Yang Li[a,1,2], Xu Feng[a,2], Seok-Hyun Yun[a,b,*]

[a] Harvard Medical School and Wellman Center for Photomedicine, Massachusetts General Hospital, 50 Blossom St., Boston, MA 02114, USA
[b] Harvard-MIT Division of Health Sciences and Technology, Cambridge, MA 02139, USA

ARTICLE INFO

Article history:
Received 9 August 2023
Revised 9 November 2023
Accepted 8 December 2023
Available online xxx

Keywords:
Cornea
Nonlinear anisotropy
Optical coherence elastography
Tissues *in vivo*

ABSTRACT

Understanding corneal stiffness is valuable for improving refractive surgery, detecting corneal abnormalities, and assessing intraocular pressure. However, accurately measuring the elastic properties, specifically the tensile and shear moduli that govern mechanical deformation, has been challenging. To tackle this issue, we have developed guided-wave optical coherence elastography that can simultaneously excite and analyze symmetric (S0) and anti-symmetric (A0) elastic waves in the cornea at around 10 kHz frequencies, enabling us to extract tensile and shear properties from measured wave dispersion curves. We verified the technique using elastomer phantoms and ex vivo porcine corneas and investigated the dependence on intraocular pressure using acoustoelastic theory that incorporates corneal tension and a nonlinear constitutive tissue model. In a pilot study involving six healthy human subjects aged 31 to 62, we measured shear moduli (Gzx) of 94±20 kPa (mean±standard deviation) and tensile moduli (Exx) of 4.0±1.1 MPa at central corneas. Our preliminary analysis of age-dependence revealed contrasting trends: -8.3±4.5 kPa/decade for shear and 0.30±0.21 MPa/decade for tensile modulus. This OCE technique has the potential to become a highly useful clinical tool for the quantitative biomechanical assessment of the cornea.

Statement of Significance

This article reports an innovative elastography technique using two guided elastic waves, demonstrating the measurement of both tensile and shear moduli in human cornea in vivo with unprecedented precision. This technique paves the way for comprehensive investigations into corneal mechanics and holds clinical significance in various aspects of corneal health and disease management.

© 2023 Acta Materialia Inc. Published by Elsevier Ltd. All rights reserved.

1. Introduction

The mechanical properties of the cornea play an essential role in establishing biomechanical homeosis with intraocular pressure (IOP) and maintaining normal corneal shapes. Measuring corneal biomechanics is significant in various aspects of corneal health and disease management, including the development of diagnostic metrics for early detection of keratoconus, monitoring corneal crosslinking, and accurately predicting corneal shapes after refractive surgeries.

The stromal tissue of the cornea has a lamellar microstructure consisting of the collagen fiber network and interfibrillar matrix [1–3]. This unique microstructure make the cornea mechanically anisotropic and approximately transverse isotropic [4]. The tensile modulus along the corneal plane is predominantly influenced by the tensile modulus of the collagen fibrils, whereas the out-of-plane shear modulus is largely dictated by the shear modulus of the extrafibrillar matrix. Therefore, measurements for both tensile and shear moduli would be essential for an accurate characterization of corneal biomechanics.

However, current techniques have severe limitations in measuring tensile and shear moduli *in vivo*. Mechanical tools, such as stress-strain tests and torsional tests, are invasive and not easily configurable for *in vivo* measurements. Two commercial instruments, namely the Ocular Response Analyzer (Reichert) [5] and Corvis ST (Oculus) [6,7], provide phenomenological, biomechanical indices through the inverse analysis of corneal deformation against

* Corresponding author.
E-mail address: syun@hms.harvard.edu (S.-H. Yun).
[1] Current address: Department of Mechanics and Engineering Science, College of Engineering, Peking University, Beijing 100871, China.
[2] Equal contribution.

https://doi.org/10.1016/j.actbio.2023.12.019
1742-7061/© 2023 Acta Materialia Inc. Published by Elsevier Ltd. All rights reserved.

Please cite this article as: G.-Y. Li, X. Feng and S.-H. Yun, Simultaneous tensile and shear measurement of the human cornea in vivo using S0- and A0-wave optical coherence elastography, Acta Biomaterialia, https://doi.org/10.1016/j.actbio.2023.12.019

air-puffs but do not explicitly generate elastic modulus information. Corneal indentation can, in principle, measure tensile modulus, but with compromised accuracy [8,9]. Brillouin microscopy can measure longitudinal modulus with high resolution [10,11], but this elastic property is not directly related to tensile and shear properties required to describe corneal deformation. Ultrasound elastography [12] and optical coherence elastography (OCE) [13–17] have been applied to the cornea *in vivo*. To date, these techniques have employed almost exclusively the antisymmetric (A0) elastic wave, whose velocity is predominantly governed by out-of-plane shear modulus [18]. In-plane tensile moduli of the cornea has been estimated from the velocity dispersion [18] or the displacement profile [19] of the A0 wave, but with relatively large fitting uncertainties.

In this work, we demonstrate a noninvasive elastography method to quantify both the tensile and shear moduli of the cornea using guided elastic waves. We employ a high-frequency OCE technique to simultaneously generate symmetric (S0) as well as antisymmetric A0 guided waves in the cornea and measure their propagation speeds. We adopt an acoustoelastic wave model that incorporates IOP-induced tension, tissue anisotropy, and nonlinearities. We then obtain tensile and shear moduli directly by fitting the model to the measured dispersion curves of the S0 and A0 waves. After testing this technique using phantoms and porcine corneas, we apply it to *in vivo* human corneas.

2. Theory of guided elastic waves

2.1. Mechanical model of the cornea

The deformation of tissue in response to mechanical stress is governed by its tensile and shear properties. The stroma dominates the overall stiffness of the cornea, accounting for approximately 90 % of its total thickness [20]. The stroma consists of 200–300 lamellar layers containing collagen fibrils aligned along the layers (Fig. 1A), which are typically orthogonally stacked between adjacent lamellas [21]. The collagen fibers bear the tensile stress induced by the IOP [22,23]. The in-plane tensile stress σ can be estimated using the Young-Laplace equation:

$$\sigma = \text{IOP} \times R/(2h), \tag{1}$$

where R and h denote the radius and thickness of the cornea, respectively (Fig. 1B).

Given the corneal microstructure, it is reasonable to adopt the Holzapfel-Gasser-Ogden (HGO) model [24], which has been widely used for mechanical modeling of arterial walls. The strain energy function of the HGO model can be written as:

$$W = \frac{\mu}{2}(I_1 - 3) + \frac{k_1}{k_2}\sum_{i=1}^{2}\left\{e^{k_2[\kappa(I_1-3)+(1-3\kappa)(I_{4i}-1)]^2} - 1\right\}, \tag{2}$$

where μ, k_1, k_2 and κ are constitutive parameters. μ represents the initial shear modulus, k_1 represents the anisotropic tensile response, and k_2 describes the nonlinear stiffening effect of collagen fibrils at large strain. κ characterizes the dispersion of collagen fibrils. $0 \le \kappa \le 1/3$, where $\kappa = 0$ is for unidirectionally aligned fibrils and $\kappa = 1/3$ corresponds to randomly distributed fibrils. According to previous studies [25,26], the collagen fibrils of central corneas are approximately aligned in two orthogonal directions along the superior-inferior and nasal-temporal axes, giving κ values lower than 0.13. In our study, we assumed $\kappa = 0$ for simplicity. The influence of corneal curvature on wave speed is negligible (see Supplementary Fig. S1). Therefore, we can use Cartesian coordinates (x_1, x_2, x_3) as shown in Fig. 1C. The axes of the collagen fibrils are denoted by $M = (1, 0, 0)^{\mathrm{T}}$ and $M' = (0, 0, 1)^{\mathrm{T}}$. The invariants in Eq. (2), I_1, I_{41} and I_{42}, can be defined by M, M', and the deformation gradient F: $I_1 = \mathrm{tr}(F^TF)$, $I_{41} = (FM)\cdot(FM)$, $I_{42} = (FM')\cdot(FM')$ [24]. The Cauchy stress tensor can be determined using $\sigma_{ij} = F_{iI}\partial W/\partial F_{jI} - p\delta_{ij}$, where p is a Lagrange multiplier for material incompressibility, δ_{ij} is the Kronecker delta, and the Einstein summation convention is used for $I \in \{1, 2, 3\}$. For biaxial stress σ, which corresponds to in-plane corneal tension, the deformation strain tensor is $F = \mathrm{diag}(\lambda, \lambda^{-2}, \lambda)$, where λ is the stretch ratio along x_1 and $\det(F) = 1$ due to the incompressibility of tissue. λ is obtained from

$$\sigma = F_{1I}\frac{\partial W}{\partial F_{1I}} - F_{2I}\frac{\partial W}{\partial F_{2I}}. \tag{3}$$

To estimate corneal tension, we consider a typical corneal radius of curvature (R) of 7.5 mm and a corneal thickness (h) of 0.53 mm. For illustration, we considered previously reported values of $\mu = 60$ kPa, $k_1 = 50$ kPa, $k_2 = 200$, and $\kappa = 0$ [25], although we later find that this k_1 value is underestimated for human corneas. Fig. 1D illustrates the variations of stress σ and stretch ratio λ for a range of IOP from 0 to 40 mmHg. Due to the nonlinear mechanical properties, the stiffness of the cornea increases with tensile strain, and the stretch ratio λ exhibits a decreasing slope as IOP increases.

We focus on the elastic waves guided in the cornea. In our OCE experiments, the vibration amplitudes of the elastic waves are only around 100 nm. Thus, the wave motion can be considered an incremental, linear perturbation on the prestressed configuration of the cornea, governed by the wave equation:

$$\alpha\frac{\partial^4\psi}{\partial x_1^4} + 2\beta\frac{\partial^4\psi}{\partial x_1^2\partial x_2^2} + \gamma\frac{\partial^4\psi}{\partial x_2^4} = \rho\left(\frac{\partial^4\psi}{\partial x_1^2\partial t^2} + \frac{\partial^4\psi}{\partial x_2^2\partial t^2}\right), \tag{4}$$

where ρ is the density, ψ is related to the displacement components induced by wave motion (u_1 and u_2) as $u_1 = \partial\psi/\partial x_2$ and $u_2 = -\partial\psi/\partial x_1$. The coefficients α, β, and γ are determined by the strain energy function and λ (see Refs. [27,28] and Supplementary Note 1). The upper boundary (epithelium) interfacing with the air is stress-free, while the lower boundary (endothelium) is in contact with the aqueous humor. By solving Eq. (4) together with the linear acoustic equation of fluid (aqueous humor) and considering the appropriate boundary conditions, we obtain a secular equation that describes the wave velocity dispersion of the guided waves in the cornea (Supplementary Note 1).

2.2. The guided waves and elastic moduli

According to the Lamb wave theory [29,30], the plate geometry of the cornea supports two fundamental guided waves with symmetric (S0) and antisymmetric (A0) motions, respectively. The S0 mode is an extensional, dilatational wave with its velocity largely governed by tensile modulus along the propagation direction. The A0 mode is a flexural, bending wave with its velocity governed by out-of-plane shear modulus. We use $\bar{G}_{zx}$ and $\bar{E}_{xx}$ to denote the out-of-plane shear modulus and in-plane tensile modulus, respectively, under the prestress condition set by the corneal tension. Under a stress-free condition (i.e., zero corneal tension, $\sigma = 0$), $\bar{G}_{zx}$ reduces to an intrinsic shear modulus $G_{zx}^{\sigma=0}(=\mu)$, and $\bar{E}_{xx}$ reduces to intrinsic Young's modulus $E_{xx}^{\sigma=0}(=4\mu+4k_1)$ (see Supplementary Note 2). For isotropic materials ($k_1 = 0$), $E_{xx}^{\sigma=0}$ is equal to 4μ. We introduce a ratio, $\bar{E}_{xx}/4\bar{G}_{zx}$ as an anisotropy index. For isotropic and stress-free materials, the ratio is equal to 1, but $\bar{E}_{xx}/4\bar{G}_{zx} \gg 1$ is expected for highly anisotropic materials, such as the cornea.

Fig. 1E shows the theoretical dispersion curves of the A0 and S0 waves as a function of frequency for two different IOP levels of 0 and 15 mmHg, respectively. At zero frequency, the velocity of the A0 wave is zero (even at 15 mmHg due to the presence of the aqueous humor). At 0 mmHg IOP, the S0 wave speed in the low frequency limit is equal to $\sqrt{E_{xx}^{\sigma=0}/\rho}$. (see Supplementary Note 2). For the highly anisotropic corneal tissue, the

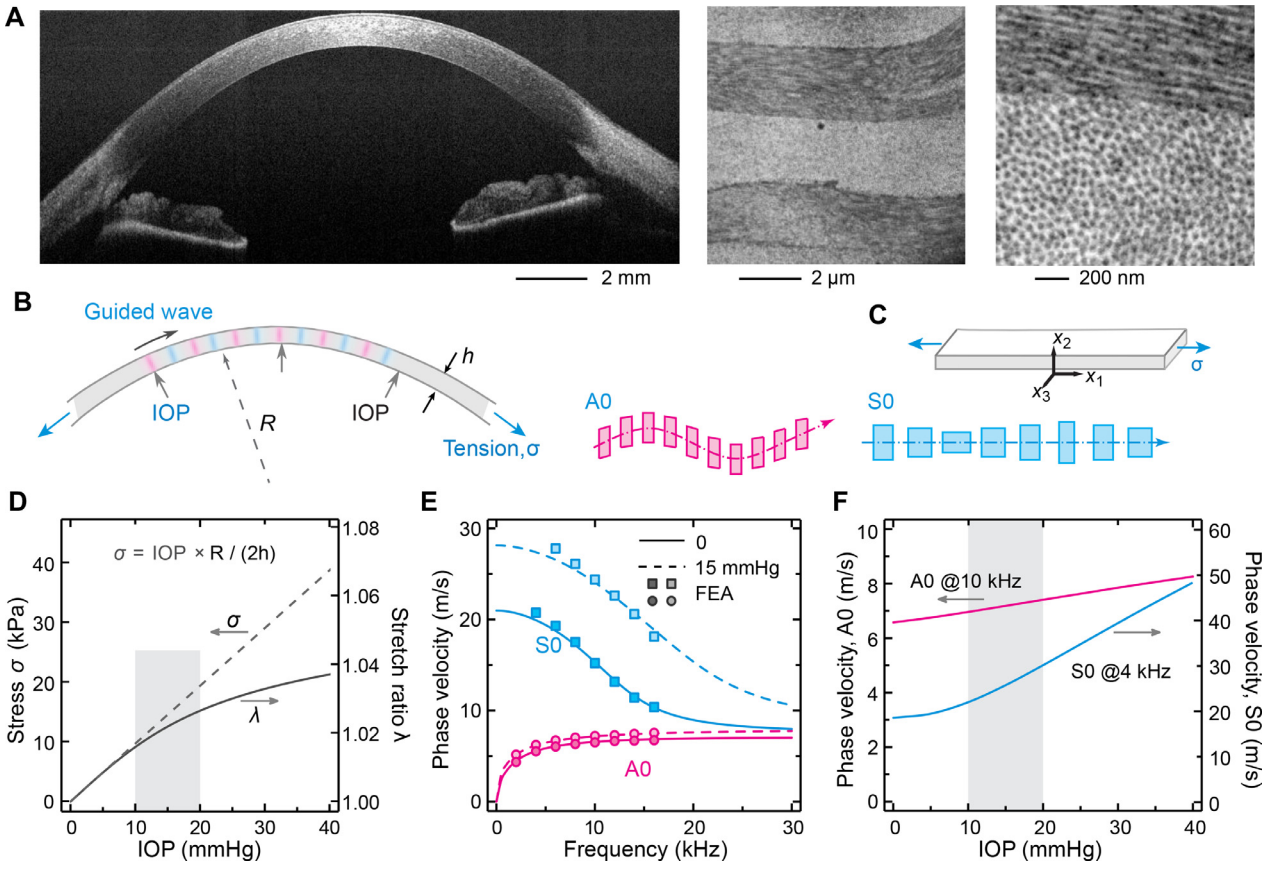

Fig. 1. Mechanical model for elastic wave motion in the cornea. (A) (left) OCT image of a healthy human volunteer and (right) electron micrographs of a porcine corneal tissue showing the microstructure of the stroma layer. (B) Static load of the cornea in physiological condition and the elastic wave motion. The fundamental guided modes are asymmetric (A0) and symmetric (S0), respectively. Boxes illustrate specific tissue deformations involved in the wave motion. (C) The coordinate system used in the model. (D) Stress σ and stretch ratio λ of the cornea under different IOP levels. The normal physiological range of the IOP is typically 10–20 mmHg (gray area). (E) Theoretical dispersion relations of the A0 and S0 modes at zero IOP (solid lines) and 15 mmHg (dashed lines). The markers show the results obtained from finite element analysis (FEA). (F) Effect of the IOP on the phase velocities of A0 (10 kHz) and S0 (4 kHz) modes for a weakly anisotropic material with $R = 7.5$ mm, $h = 0.53$ mm, $\mu = 30$ kPa, $k_1 = 50$ kPa, $k_2 = 200$, and $\kappa = 0$.

plane shear modulus $E_{xx}^{\sigma=0}$ is nearly equivalent to uniaxial tensile modulus or Young's modulus. On the other hand, in the high frequency regime where the wavelengths become shorter than the corneal thickness, both the A0 and S0 velocities converge to plateaus. At zero tension, the asymptotic velocities are close to $\sqrt{\mu/\rho}$ (see Supplementary Note 2). The corneal tension increases the high-frequency asymptotic plateaus through its effects on the material properties and acoustic deformation (see Supplementary Note 2).

For illustration, in Fig. 1F we plot the phase velocities of the A0 mode at 10 kHz and the S0 mode at 4 kHz as a function of the IOP level for the modestly anisotropic material parameters ($\mu = 60$ kPa, $k_1 = 50$ kPa, $k_2 = 200$). We find that the phase velocity of A0 mode varies approximately linearly with IOP with a slope of $\sim$ 0.04 m/s•mmHg ($r^2 > 0.99$). On the other hand, the S0 wave speed is nearly insensitive to IOPs lower than 10 mmHg, but increases with IOPs greater than 15 mmHg with a slope of $\sim$ 0.91 m/s•mmHg ($r^2 > 0.99$). The S0 wave is more sensitive than the A0 wave to IOP in the physiological range because of the large exponential nonlinearity of tensile elasticity against the corneal tension. It should be noted that the tension affects the wave velocities not only through the nonlinear material properties but also directly through the tension-induced restoring forces on the wave displacements. The acoustoelastic analysis using α, β, and γ effectively decomposes the two mechanisms and allows us to extract the elastic moduli from the wave velocities (Supplementary Note 1).

3. Methods

3.1. OCE system

We used a custom-built, swept-source phase-sensitive optical coherence tomography (OCT) imaging system [13,31]. The OCT system has a center wavelength of 1300 nm and a bandwidth of 80 nm at an A-line rate of 43.2 kHz, offering an axial resolution of $\sim$ 15 μm. The illumination power on the cornea is below 10 mW in compliance with the ANSI Z136.1-2014 safety standard. Trigger pulses generated from a narrowband fiber-optic Bragg grating (i.e., lambda trigger) ensures time synchronization for the OCT data acquisition, beam scanning, and wave generation. The displacements of the guided waves were measured using the method previously described [13,30]. Briefly, continuous pure tone stimuli were used with frequencies varied from 2 to 16 kHz with an interval of 2 kHz. At each transverse location of the optical beam, 172 A-lines were acquired, which constitutes a single M-scan data. A total of 96 transverse positions along the sample are scanned. The data acquisition time was about 0.4 s at each frequency.

We extracted displacement profiles over time t, and then performed a Fourier transform to move the data from time t domain to frequency f domain. The phase and amplitude of the mechanical vibration at the driving frequency were determined. This lock-in detection effectively reduces noises and eliminates any phase changes by subject's motion in other frequencies outside the lock-in bandwidth (250 Hz) around the excitation frequency. To cal-

culate the surface wave speeds, we obtained 1-dimensional displacement profiles from the top surface of the sample, and applied a Fourier transform to measure the wavenumber k of each wave. Two most prominent peaks in the k_x domain were identified using a global search algorithm and assigned to the A0 and S0 waves. Only one primary peak associated with the A0 wave could appear at low frequencies. This analysis in the spatial frequency domain is critical to remove other higher-order modes especially at high frequencies [32]. The phase velocity is determined by $v = 2\pi f/k$. To minimize the effect from residual corneal vibration from the prior frequency, the first A-line in the M-scan was ignored in post-processing. The surface ripple artifacts were eliminated in post data processing using the approach detailed in Ref [33].

The noise equivalent amplitude sensitivity was measured to be ~ 4 nm per A-line, or 19 pm/$\sqrt{Hz}$, for an optical SNR of 30 dB at the surface of sample. With the 172 A-line M-mode lock-in integration (over 4 ms or 250 Hz), the effective sensitivity becomes 300 pm. The ultimate OCE sensitivity is further enhanced by the spatial analysis over 96 locations. Without wave attenuation, the maximum sensitivity would be ~ 31 pm. The typical vibration amplitude used in the experiments was larger than 20 nm. The resulting high signal to noise ratio allows the wavenumber to be determined with high precision ($<<$ 1 %).

3.2. Optimization of the wave-excitation probe

To generate both the A0 and S0 waves in the cornea, we utilized a custom-designed vibrating probe consisting of a piezoelectric transducer (PZT) and a probe tip, as depicted in Fig. 2B. We tested different tilt angles of the probe ($\alpha = 0$, 15, and 30 degrees) and found that the highest A0 amplitude at $\alpha = 0$ deg and the lowest A0 amplitude at $\alpha = 30$ deg. On the other hand, the S0 amplitude was the maximum at $\alpha = 15$ deg (Supplementary Fig. S3B). Considering that S0 wave dispersion data above 10 kHz are critical, we selected the tilt angle of 15 degrees and employed this configuration for all subsequent experiments.

Using the Hertz model of elastic contact, we calculated the contact length of the tip on the corneal surface to be $\sim$ 520 µm. To verify this, we put ink on the tip of the probe and measured the length of the ink transfer mark to a phantom. Our result was approximately 500 µm in good agreement with the theoretical prediction. According to the Hertz model, the indentation depth of the probe tip onto the corneal tissue should be around 100 µm.

3.3. Statistical analysis

We report the wave speed data as mean ± standard deviation (std) for the phantom, *ex vivo* porcine corneas, and *in vivo* human corneas. To highlight the inter-sample variation of the porcine samples, we report the data as boxplots indicating the median, the 25th percentile (Q1) and the 75th percentile (Q3). The whisker extends from the hinge to the largest or smallest value no further than 1.5 times the interquartile range of the hinge. The 95 % confidence interval, mean and SD were calculated for the *in vivo* human data across the age span.

4. Results

4.1. Validation using phantoms

To validate the OCE method, we conducted experiments using a 0.45-mm thick polydimethylsiloxane (PDMS) sheet, which is an isotropic material. The PDMS sheet was mounted in an artificial anterior chamber, as illustrated in Fig. 2C. Initially, no pressure or in-plane stress was applied to the PDMS sheet. Displacement maps and surface displacement profiles were obtained at 4 kHz and 12 kHz, as shown in Fig. 2D and E, respectively. In the wavenumber domain (Fig. 2F), two distinct peaks were observed. The peak at the lower wavenumber corresponded to the S0 mode with a higher phase velocity, while the peak at the higher wavenumber corresponded to the A0 mode with a lower velocity. The A0 wave was clearly detected across all frequencies ranging from 2 to 16 kHz. However, the S0 wave was reliably identified only at frequencies of 6 kHz and above and was not consistently observed at 2 and 4 kHz due to the relatively short contact length of the probe tip (0.5 mm) compared to the S0 half wavelengths ($\sim$3.5 mm at 4 kHz). The corresponding phase velocity dispersion curves are depicted in Fig. 2G, showing good agreement between the experimental data and our theoretical model. For this tension-free, isotropic PDMS phantom, we determined the intrinsic shear modulus $G_{zx}^{\sigma=0} = \mu =$ 184 kPa and $E_{xx}^{\sigma=0} = 736$ kPa. These values satisfy the expected relationship $E_{xx}^{\sigma=0} = 4\mu$, which holds only for isotropic materials. We then cut the sample into small pieces and performed uniaxial tensile tests using a commercial mechanical machine (see Supplementary Fig. S4). By curve fitting of the strain-stress curve we measured a quasi-static shear modulus of 172 kPa. This value is quite close to 184 kPa obtained from OCE at around 10 kHz frequencies.

To investigate the effect of intraocular pressure (IOP), we increased the IOP from 0 to 40 mmHg by attaching a water column with controlled height to the artificial anterior chamber. Fig. 2H presents the A0 wave velocity at 16 kHz as a linear function of IOP, demonstrating a linear slope of 0.02 m/s•mmHg, or 0.2 % increase per mmHg. This slope aligns with the theoretical expectation for a neo-Hookean model of PDMS ($\mu = 184$ kPa, $k_1 = 0$).

4.2. Porcine corneas ex vivo

To further validate the OCE method, we conducted experiments using fresh porcine eye globes *ex vivo*, where the IOP was controlled using a saline water column, as shown in Fig. 3A. Displacement maps were obtained at frequencies of 2 kHz, 4 kHz, and 6 kHz at an IOP of 5 mmHg, as depicted in Fig. 3B. Corresponding displacement profiles at the cornea surface are presented in Fig. 3C. In the wavenumber domain, both the A0 and S0 modes were clearly identified, with the S0 mode becoming dominant at higher frequencies. By fitting the measured dispersion curves over frequency (Fig. 3E), we determined an *in situ* out-of-plane shear modulus of $\bar{G}_{zx} = 9.0 \pm 0.6$ kPa and an *in situ* in-plane tensile modulus of $\bar{E}_{xx} = 216 \pm 22$ kPa. The ratio $\bar{E}_{xx}/4\bar{G}_{zx}$ is 6, indicating a significant tensile-to-shear anisotropy in the corneal tissue. Fig. 3F displays the wave velocities measured at 2 kHz and 10 kHz from seven porcine eye globe samples. The mean phase velocities for the A0 and S0 modes at 2 kHz were 2.18 ± 0.08 m/s and 17.9 ± 6.1 m/s (Mean ± SD), respectively, while the A0 wave velocity at 10 kHz was 3.46 ± 0.19 m/s.

The dependence of phase velocity on IOP was investigated by increasing the IOP from 5 mmHg up to 40 mmHg in increments of 5 or 10 mmHg. The deformation of the cornea, as measured from the OCT images, exhibited good agreement with our numerical simulations (Supplementary Fig. S5). Fig. 3G illustrates the IOP-dependence of the A0 wave at 10 kHz, demonstrating a linear relationship. The velocity slope was found to be 0.12 m/s·mmHg or a 2.5 % increase per mmHg at 15 mmHg. Fig. 3H displays the IOP-dependence of the S0 wave at 2 kHz. The S0 wave velocity exhibited nonlinearity initially up to 10 mmHg, followed by a linear increase with larger IOPs. The slope at 15 mmHg was approximately 0.93 m/s·mmHg, or 3.3 % increase per mmHg. The experimental data exhibited remarkable agreement with numerical simulation results based on the model with $\mu = 9$ kPa and $k_1 = 45$ kPa. A

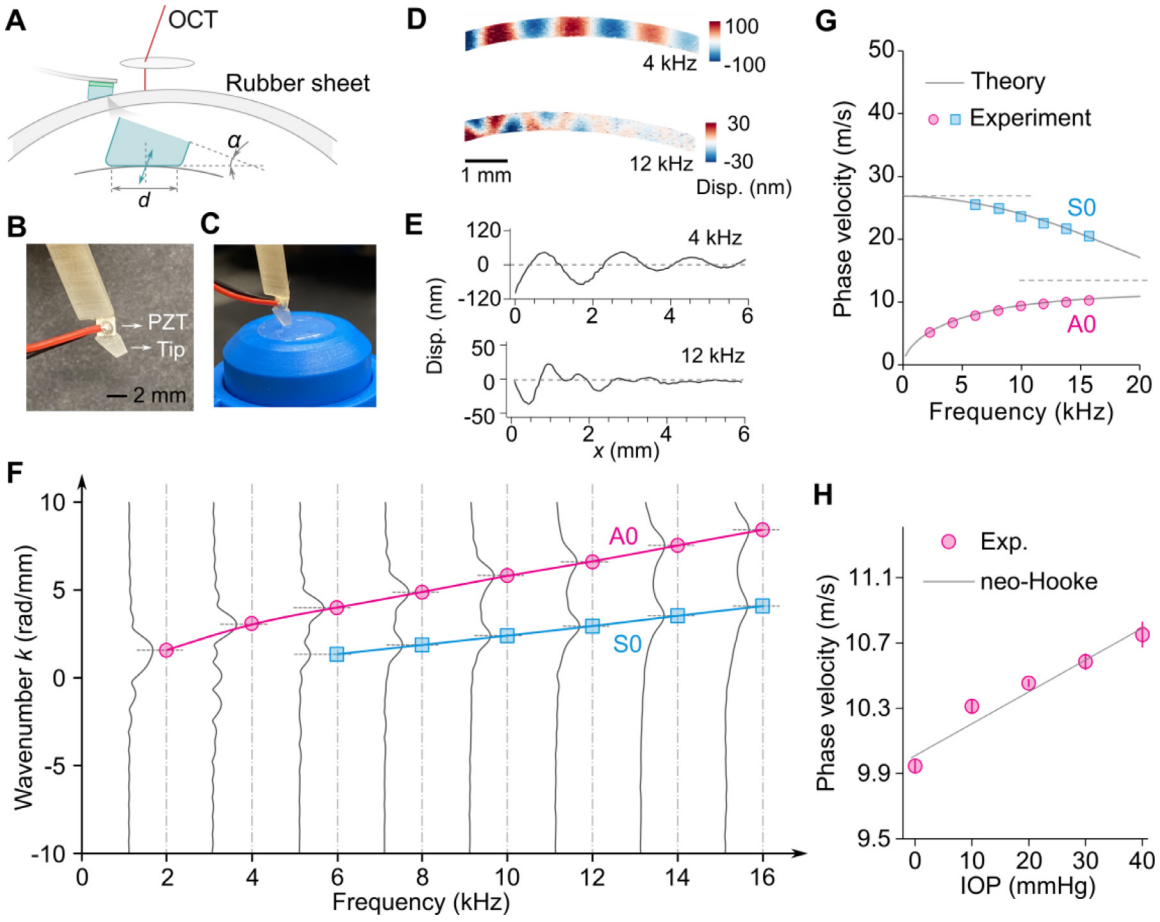

Fig. 2. Verification using elastomer phantoms. (A) Schematic of the experimental setup including the contact piezoelectric probe with a tilt angle α between the vibration direction and the surface normal. (B) Picture of the contact probe. (C) Picture of the PDMS sheet phantom on an artificial anterior chamber. (D) Displacement maps at 4 kHz and 12 kHz (IOP = 0 mmHg). (E) Corresponding surface displacement profiles. Only the real parts are shown. (F) Fourier transformations of the surface displacement profiles to measure the dispersion relations. The S0 mode is clearly identified at 6 -16 kHz. (G) Phase velocity dispersion relations and the theoretical model. (H) Effect of IOP on the A0 wave velocity at 16 kHz. The line represents the theoretical fit based on the neo-Hookean model ($k_1 = 0$).

Table 1
In vivo human data.

Subjects	Age	Gender	Spherical diopters	Corneal thickness (mm)	Out-of-plane shear modulus $\bar{G}_{zx}$ (kPa)	In-plane tensile modulus $\bar{E}_{xx}$ (kPa)	$\bar{E}_{xx}/4\bar{G}_{zx}$
1	31	M	−3.00	0.55	81 ± 3	3730 ± 57	11.5
2	34	F	−1.50	0.50	93 ± 12	3060 ± 270	8.3
3	33	M	−2.50	0.55	99 ± 7	3510 ± 460	8.9
4	34	M	−7.75	0.60	130 ± 10	3980 ± 500	7.7
5	62	M	−3.00	0.55	70 ± 3	3400 ± 140	12.0
6	53	M	−5.75	0.57	89 ± 2	6060 ± 870	22.4

slightly higher value of 500 was used for k_2 to account for the nonlinearity of corneal tissues.

4.3. Human corneas in vivo

In the final phase of our study, we applied the OCE method to human eyes. Six healthy subjects with normal IOP in a range of 10-15 mmHg were recruited. Four subjects were in early 30s (31-34 years old), and two subjects were over 50s (53 and 62 years old). Details about the subjects can be found in Table 1. The study was conducted at the Massachusetts General Hospital (MGH) with approval from the Institutional Review Board (IRB) of MGH and the Mass General Brigham Human Research Office. A topical anesthetic was administered to the eye. Only the left eye of each subject was measured. The excitation contact probe used was spring-loaded to maintain a small, constant force of ~10 mN when in contact with the corneal surface (Fig. 4A). No noticeable corneal deformation was observed in OCT images. A complete scan from 6 to 16 kHz, with a 2 kHz interval, took 2.4 s. All subjects demonstrated cooperation by refraining from blinking and maintaining focus on a fixed target during the imaging scan.

Fig. 4B presents representative displacement profiles obtained from Subject 1. At 6 kHz, only the A0 mode was excited, while at 12 kHz and above, a combination of the S0 and A0 mode was observed. Measured surface wave displacement profiles are shown in Fig. 4C, and the corresponding wavenumber domain plots are displayed in Fig. 4D. At 16 kHz, peaks appearing in the negative wavenumber domain are likely caused by the reflection of the S0 wave from the limbus and were therefore disregarded.

Fig. 4E depict the measured phase velocity dispersion curves for the six healthy human subjects. Each data point and error bar represent the mean and standard deviation of two consecutive OCE

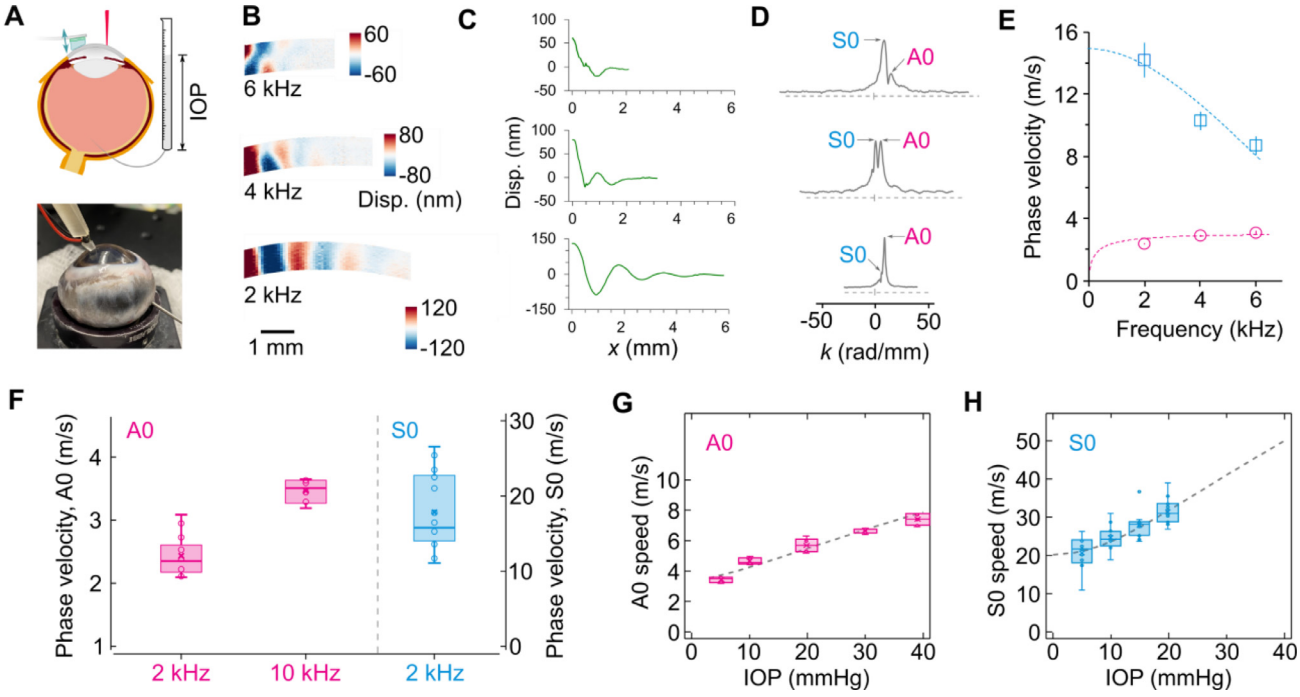

Fig. 3. Simultaneous measurement of the A0 and S0 waves in ex vivo porcine corneas. (A) Schematic of the experimental setup. IOP is controlled using a water column. (B) Maps of the displacement field. (C) Surface displacement extracted from the surface of the cornea at 2, 4, and 6 kHz (bottom to top). (D) Fourier transform of the displacement. The two peaks correspond to A0 and S0 modes, respectively. (E) Corresponding dispersion relations of the A0 and S0 waves. The error bar represents three measurements on the same location of the porcine cornea. (F) Inter-sample variations from 7 samples. (G) Effect of the IOP on the phase velocities of the A0 mode at 10 kHz. (H) Effect of the IOP on the phase velocities of the S0 mode at 2 kHz. Dashed curves represent the theoretical fit.

scans performed at the same location. The wavelengths of the A0 and S0 waves are displayed in Appendix Table A1. At 12 kHz and above, the contact length (~0.5 mm) is notably larger than the half of the A0 wavelength, resulting in the suppression of the A0 wave. This is consistent with the observation that the S0 mode becomes more pronounced at and above 12 kHz. For Subject 6, the S0 mode was only observed at 16 kHz due to its long wavelengths at lower frequencies compared to the contact length.

The dispersion curves were fitted with the acoustoelastic model described in Section 2, assuming an IOP of 12 mmHg for all subjects. The measured shear and tensile modulus values are shown in Table 1. For Subjects 1 to 4 (31 - 34 yo), we obtained shear modulus $\bar{G}_{zx}$ in a range of 81 to 130 kPa, and tensile modulus $\bar{E}_{xx}$ varying from 3.06 to 3.98 MPa. The anisotropy ratio $\bar{E}_{xx}/4\bar{G}_{zx}$ ranges from 7.7 to 11.5. Subjects 5 and 6 (62 and 53 yo) exhibited shear moduli ($\bar{G}_{zx}$) of 70 and 89 kPa and tensile moduli ($\bar{E}_{xx}$) of 3.40 and 6.06 MPa, respectively. The ratios $\bar{E}_{xx}/4\bar{G}_{zx}$ were 12.0 and 22.4, higher than Subjects 1 to 4. Fig. 4F shows the measured shear and tensile moduli as a function of the age. A linear regression analysis revealed a negative slope of -8.3 ±4.5 kPa per decade for shear modulus and a positive slope of 303 ± 206 kPa per decade for tensile modulus (95 % confidence interval).

5. Discussion

In this study, we presented a guided-wave OCE system that enabled simultaneous excitation and detection of the S0 and A0 waves in corneas. While the relationship between the waves and elastic moduli has been known, to our knowledge, this is the first experimental study that measures tensile modulus directly from the S0 wave in the cornea. The measured wave dispersion and dependence on pre-stress (corneal tension) showed good agreement with our acoustoelastic theory based on the HGO constitutive model. By fitting the phase velocity dispersion curves of the S0 and A0 waves using the model, we obtained the in-plane tensile modulus and out-of-plane shear modulus of human corneas *in vivo*. From six normal subjects, the shear modulus ($\bar{G}_{zx}$) ranged from 70 to 130 kPa and the tensile modulus ($\bar{E}_{xx}$) ranged from 3.06 to 6.06 MPa.

In terms of the HGO model parameters, we determined that k_1 ranged from 670 to 1420 kPa and k_2 was set to 500, based on the data collected from the six subjects. While the HGO model is considered a reasonable choice for describing corneal behavior, ongoing efforts to develop more sophisticated constitutive models are underway [34,35]. It would be interesting to incorporate these models into the acoustoelastic theory and derive parameters from our OCE data. However, this topic falls beyond the scope of the current study.

Comparing our results with previous mechanical measurements on *ex vivo* corneal tissues, tensile moduli have been reported in the range of 0.2 to 3 MPa [36–38], while torsional tests applying shear stress along the corneal plane exhibited elastic moduli ranging from 3 to 50 kPa [39,40]. Our *in vivo* results measured at ~ 10 kHz are slightly higher than these *ex vivo* mechanically measured values. We also compared our data with previous *in vivo* measurements reported in the literature (see Appendix Table A2). Some studies only reported group velocities [2,15,41,42], from which it is difficult to quantify elastic moduli accurately without phase velocity dispersion information. Our measured A0 wave phase velocities were reasonably consistent with the reported values from previous OCE studies [13,16]. Our measured tensile moduli were significantly larger than previously reported values up to 0.8 MPa using indentation and tonometer-based methods [8,9]. We speculate that the indentation might cause eyeball movement and IOP change leading to an underestimation of tensile modulus.

In our current study, we observed an upward trend of tensile modulus with age *in vivo*. This age-dependent stiffening is qualitatively consistent with previous results of *ex vivo* mechanical stud-

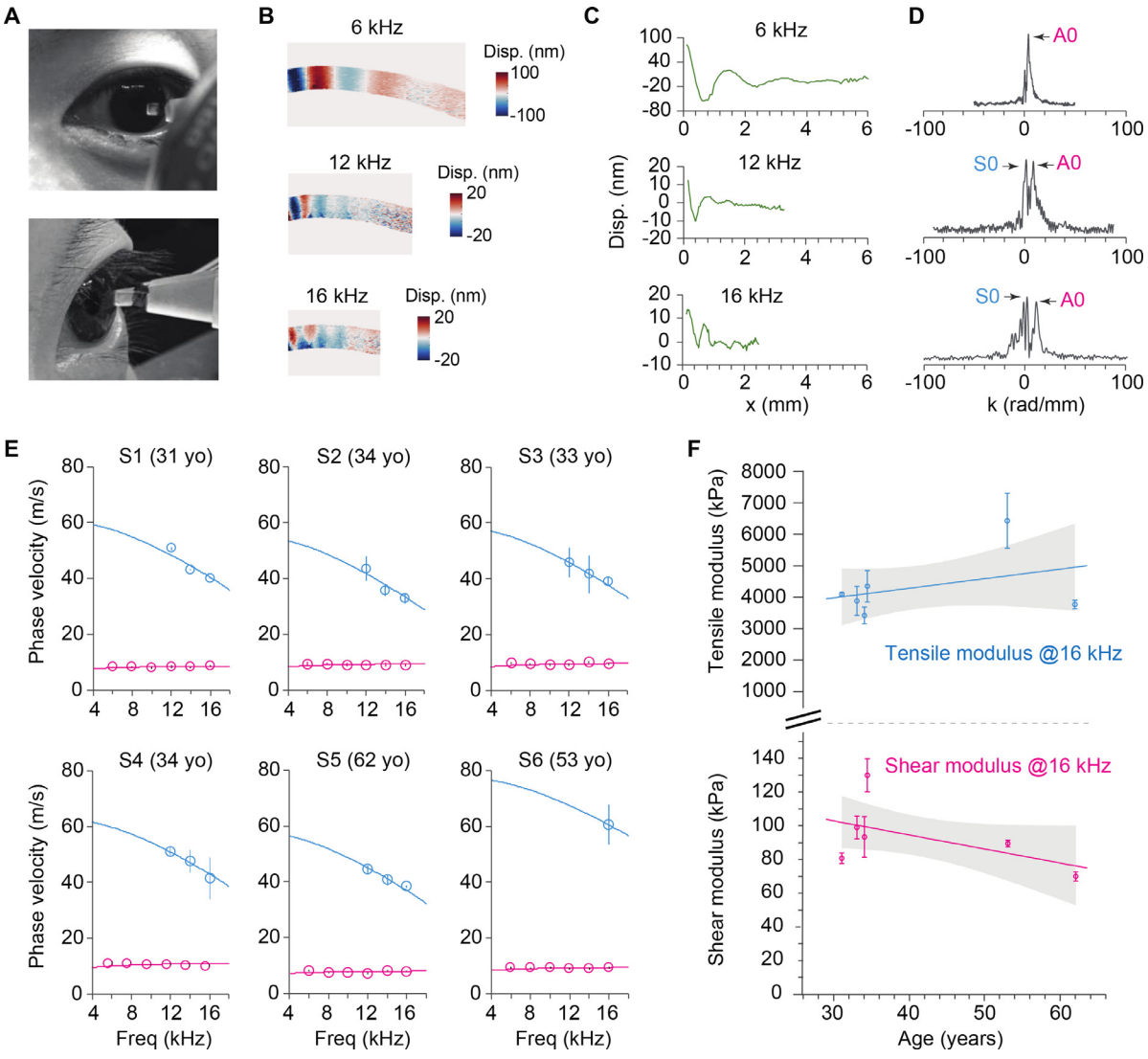

Fig. 4. In vivo human measurement of the tensile and shear moduli using the S0 and A0 waves. (A) Monitoring camera view of a human subject during measurement. (B) Displacement profiles at 6, 12, and 16 kHz for Subject 2. (C) Surface displacement. (D) Wavenumber domain Fourier transform result of the wave displacement. Arrows point to the A0 and S0 modes. (E) Dispersion curves measured from six healthy subjects. (F) Regression analysis of age dependence for the tensile and shear moduli measured at 16 kHz. Shaded regions represent 95 % confidence intervals.

ies [36–38]. This current study also observed a downward trend of shear modulus with age *in vivo*, consistently from our earlier finding [13]. The subjects above 50s exhibited 32 % *higher* tensile modulus and 21 % *lower* shear modulus (80 vs. 101 kPa) compared to the younger subjects (average age 33). This opposite trend between tensile and shear moduli is rather surprising and highly intriguing, although large-scale clinical studies are warranted not only to confirm this preliminary finding and but also to understand their implications. One plausible explanation for the opposite trend is that collagen fibers in the cornea lose elasticity and become stiffer with age, resulting in increased tensile modulus, while the interfibrillar matrix softens and diminishes shear modulus.

To capture the full dispersion curve of the S0 wave in human corneas, it is necessary to extend the frequency range beyond 16 kHz. Additionally, people with ocular hypertension and patients with high-tension glaucoma are expected to have even higher S0 wave speeds, necessitating higher frequencies for accurately characterizing the S0 waves. We have recently developed an ultrahigh-frequency OCE method [43] and plan to incorporate this technique in our future clinical studies. With further optimizations, the guided-wave OCE technique holds promise for comprehensive studies of corneal mechanics and its role in the management of corneal diseases and refractive surgeries.

Funding

National Institutes of Health (NIH) via grants (R01-EY033356, R01-EY034857).

Declaration of Competing Interest

The authors declare that they have no known competing financial interests or personal relationships that could have appeared to influence the work reported in this paper.

Supplementary materials

Supplementary material associated with this article can be found, in the online version, at doi:10.1016/j.actbio.2023.12.019.

Appendix

Table A1
Measured wavelengths of the A0 and S0 wave from six subjects.

Frequency (kHz)	A0 wavelength (mm)	S0 wavelength (mm)
6	1.54 ± 0.18	–
8	1.14 ± 0.15	–
10	0.89 ± 0.11	–
12	0.74 ± 0.10	3.93 ± 0.29
14	0.65 ± 0.07	2.98 ± 0.31
16	0.57 ± 0.05	2.63 ± 0.60

Table A2
Previous *in vivo* measurements of corneal biomechanics

Refs	Stimulus (Frequency)	Method	Subjects	Results	Model
Sit [12]	Shaker (100 Hz)	US	Human (N = 20)	Phase velocity, 1.82 ± 0.10 m/s	Lamb wave
Nguyen [2]	ARF (~800 Hz)	US	Porcine (N = 4)	Group velocity, 6 ~ 8 m/s	Lamb wave
Nguyen [41]	ARF (~800 Hz)	US	Porcine (N = 4)	Group velocity, ~1.9 m/s	Lamb wave
Ramier [13]	Contact probe (up to 16 kHz)	OCE	Human (N = 12)	Phase velocity, 7.86 ± 0.75 m/s	Rayleigh surface wave
Lan [15]	Air-puff (~500 Hz)	OCE	Human (N = 18)	Group velocity, ~3.5 m/s	-
Jin [16]	Air-puff (~500 Hz)	OCE	Human (N = 12)	Phase velocity, 12.73 ± 1.46 m/s (>2 kHz)	Scholte wave
Zvietcovich [44]	ARF (2 kHz)	OCE	Rabbit (N = 4)	Phase velocity, 3.75 ~ 5.72 m/s	Lamb wave
Mekonnen [45]	ARF (<3 kHz)	OCE	Mouse (N = 4)	Phase velocity, 3.41 ± 0.52 m/s	Lamb wave
Kirby [18]	ARF (<3 kHz)	OCE	Rabbit (N = 5)	Shear modulus 34 kPa to 261 kPa and tensile modulus 20 MPa to 44 MPa	Lamb wave
Jin [46]	ARF (~500 Hz)	OCE	Rabbit (N = 4)	Phase velocity, 7.52 ± 1.11 m/s	Rayleigh surface wave
Li [42]	ARF (~500 Hz)	OCE	Rabbit (N = 4)	Group velocity, ~6.2 m/s	-
Kling [6]	Air-puff (~30 Hz)	Corvis ST	Human (N = 9)	Young's modulus, ~0.40 MPa for posterior and ~1.52 MPa for anterior cornea	Finite element analysis
Shih [7]	Air-puff (~30 Hz)	Corvis ST	Human (N = 25)	Young's modulus, ~0.32 MPa	Modal analysis
Pye [8]	Applanation (Static)	Applanation Tonometry	Human (N = 100)	Young's modulus, 0.25 ± 0.1 MPa	Orssengo-Pye model
Lam [9]	Flat indenter (Static)	Indentation	Human (N = 29)	Tangent modulus, 0.755 ± 0.159 MPa	Thin shell model

ARF, acoustic radiation force; US, ultrasound elastography; OCE, optical coherence elastography

References

[1] A. Elsheikh, D. Alhasso, Mechanical anisotropy of porcine cornea and correlation with stromal microstructure, Exp. Eye Res. 88 (6) (2009) 1084–1091.
[2] T.M. Nguyen, J.F. Aubry, M. Fink, J. Bercoff, M. Tanter, In vivo evidence of porcine cornea anisotropy using supersonic shear wave imaging, Invest. Ophthalmol. Vis. Sci. 55 (11) (2014) 7545–7552.
[3] A.M. Eltony, Peng Shao, Seok-Hyun Yun, Measuring mechanical anisotropy of the cornea with Brillouin microscopy, Nat. Commun. 13 (2022) 1354.
[4] J.J. Pitre, M.A. Kirby, D.S. Li, T.T. Shen, R.K. Wang, M. O'Donnell, I. Pelivanov, Nearly-incompressible transverse isotropy (NITI) of cornea elasticity: model and experiments with acoustic micro-tapping OCE, Sci. Rep. 10 (2020) 12983.
[5] D.A. Luce, Determining in vivo biomechanical properties of the cornea with an ocular response analyzer, J. Cataract. Refract. Surg. 31 (1) (2005) 156–162.
[6] S. Kling, N. Bekesi, C. Dorronsoro, D. Pascual, S. Marcos, Corneal viscoelastic properties from finite-element analysis of in vivo air-puff deformation, PLoS One 9 (8) (2014) e104904.
[7] P.J. Shih, H.J. Cao, C.J. Huang, I.J. Wang, W.P. Shih, J.Y. Yen, A corneal elastic dynamic model derived from Scheimpflug imaging technology, Ophthal. Physiol. Optics 35 (6) (2015) 663–672.
[8] D.C. Pye, A clinical method for estimating the modulus of elasticity of the human cornea in vivo, PLoS One 15 (1) (2020) e0224824.
[9] A.K. Lam, Y. Hon, L.K. Leung, D.C. Lam, Repeatability of a novel corneal indentation device for corneal biomechanical measurement, Ophthal. Physiol. Optics 35 (4) (2015) 455–461.
[10] P. Shao, A.M. Eltony, T.G. Seiler, B. Tavakol, R. Pineda, T. Koller, T. Seiler, S.H. Yun, Spatially-resolved Brillouin spectroscopy reveals biomechanical abnormalities in mild to advanced keratoconus in vivo, Sci. Rep. 9 (2019) 7467.
[11] H. Zhang, L. Asroui, I. Tarib, W.J. Dupps, G. Scarcelli, J.B. Randleman, Motion tracking brillouin microscopy evaluation of normal, keratoconic, and post-laser vision correction corneas: motion tracking Brillouin microscopy in keratoconus and laser vision correction, Am. J. Ophthalmol. 254 (2023) 128–140.
[12] A.J. Sit, S.C. Lin, A. Kazemi, J.W. McLaren, C.M. Pruet, X. Zhang, In vivo non-invasive measurement of Young's modulus of elasticity in human eyes: a feasibility study, J. Glaucoma 26 (11) (2017) 967.
[13] A. Ramier, A.M. Eltony, Y. Chen, F. Clouser, J.S. Birkenfeld, A. Watts, S.H. Yun, In vivo measurement of shear modulus of the human cornea using optical coherence elastography, Sci. Rep. 10 (2020) 17366.
[14] F. Zvietcovich, J. Birkenfeld, A. Varea, A.M. Gonzalez, A. Curatolo, S. Marcos, Multi-meridian wave-based corneal optical coherence elastography in normal and keratoconic patients, Invest. Ophthalmol. Vis. Sci. (2022) 2380–A0183.
[15] G. Lan, S.R. Aglyamov, K.V. Larin, M.D. Twa, In vivo human corneal shear-wave optical coherence elastography, Optom. Vis. Sci. 98 (1) (2021) 58.
[16] Z. Jin, S. Chen, Y. Dai, C. Bao, S. Ye, Y. Zhou, Y. Wang, S. Huang, Y. Wang,

M. Shen, In vivo noninvasive measurement of spatially resolved corneal elasticity in human eyes using Lamb wave optical coherence elastography, J. Biophotonics 13 (8) (2020) e202000104.
[17] Y. Li, J. Zhu, J.J. Chen, J. Yu, Z. Jin, Y. Miao, A.W. Browne, Q. Zhou, Z. Chen, Simultaneously imaging and quantifying in vivo mechanical properties of crystalline lens and cornea using optical coherence elastography with acoustic radiation force excitation, APL Photonics 4 (10) (2019) 106104.
[18] M.A. Kirby, G. Regnault, I. Pelivanov, M. O'Donnell, R.K. Wang, T.T. Shen, Elastography for quantification of corneal anisotropic elasticity: in vivo rabbit study, Transl. Vis. Sci. Technol. 12 (3) (2023) 15.
[19] G.Y. Li, X. Feng, S.H. Yun, In vivo optical coherence elastography unveils spatial variation of human corneal stiffness, IEEE Trans. Biomed. Eng. (2023).
[20] D.W. DelMonte, T. Kim, Anatomy and physiology of the cornea, J. Cataract. Refract. Surg. 37 (3) (2011) 588–598.
[21] K.M. Meek, A.J. Quantock, The use of X-ray scattering techniques to determine corneal ultrastructure, Prog. Retin. Eye Res. 20 (1) (2001) 95–137.
[22] J.W. Ruberti, A. Sinha Roy, C.J. Roberts, Corneal biomechanics and biomaterials, Annu. Rev. Biomed. Eng. 13 (2011) 269–295.
[23] A. Kotecha, What biomechanical properties of the cornea are relevant for the clinician? Surv. Ophthalmol. 52 (6) (2007) S109–S114.
[24] T.C. Gasser, R.W. Ogden, G.A. Holzapfel, Hyperelastic modelling of arterial layers with distributed collagen fibre orientations, J. R. Soc., Interface 3 (6) (2006) 15–35.
[25] A. Pandolfi, Cornea modelling, Eye Vision 7 (2020) 2.
[26] A. Pandolfi, G.A. Holzapfel, Three-dimensional modeling and computational analysis of the human cornea considering distributed collagen fibril orientations, (2008).
[27] M. Destrade, G. Saccomandi, Waves in Nonlinear Pre-Stressed Materials, Springer Science & Business Media, 2007.
[28] G.Y. Li, Q. He, R. Mangan, G. Xu, C. Mo, J. Luo, M. Destrade, Y. Cao, Guided waves in pre-stressed hyperelastic plates and tubes: Application to the ultrasound elastography of thin-walled soft materials, J. Mech. Phys. Solids 102 (2017) 67–79.
[29] Z.L. Han, J.S. Li, M. Singh, C. Wu, C.H. Liu, R. Raghunathan, S.R. Aglyamov, S. Vantipalli, M.D. Twa, K.V. Larin, Optical coherence elastography assessment of corneal viscoelasticity with a modified Rayleigh-Lamb wave model, J. Mech. Behav. Biomed. Mater. 66 (2017) 87–94.
[30] A. Ramier, B. Tavakol, S.H. Yun, Measuring mechanical wave speed, dispersion, and viscoelastic modulus of the cornea using optical coherence elastography, Opt. Express 27 (12) (2019) 16635–16649.
[31] X. Feng, G.Y. Li, A. Ramier, A.M. Eltony, S.H. Yun, In vivo stiffness measurement of epidermis, dermis, and hypodermis using broadband Rayleigh-wave optical coherence elastography, Acta Biomater. 146 (2022) 295–305.
[32] G.Y. Li, X. Feng, A. Ramier, S.H. Yun, Supershear surface waves reveal prestress and anisotropy of soft materials, J. Mech. Phys. Solids 169 (2022) 105085.
[33] S. Song, Z. Huang, R.K. Wang, Tracking mechanical wave propagation within tissue using phase-sensitive optical coherence tomography: motion artifact and its compensation, J. Biomed. Opt. 18 (12) (2013) 121505.
[34] T. Liu, M. Shen, H. Li, Y. Zhang, B. Mu, X. Zhao, Y. Wang, Changes and quantitative characterization of hyper-viscoelastic biomechanical properties for young corneal stroma after standard corneal cross-linking treatment with different ultraviolet-a energies, Acta Biomater. 113 (2020) 438–451.
[35] S. Wang, S.A. Chester, Multi-physics modeling and finite element formulation of corneal UV cross-linking, Biomech. Model. Mechanobiol. 20 (4) (2021) 1561–1578.
[36] A. Elsheikh, D. Wang, M. Brown, P. Rama, M. Campanelli, D. Pye, Assessment of corneal biomechanical properties and their variation with age, Curr. Eye Res. 32 (1) (2007) 11–19.
[37] G. Wollensak, E. Spoerl, T. Seiler, Stress-strain measurements of human and porcine corneas after riboflavin–ultraviolet-A-induced cross-linking, J. Cataract. Refract. Surg. 29 (9) (2003) 1780–1785.
[38] N.E.K. Cartwright, J.R. Tyrer, J. Marshall, Age-related differences in the elasticity of the human cornea, Invest. Ophthalmol. Vis. Sci. 52 (7) (2011) 4324–4329.
[39] S.J. Petsche, D. Chernyak, J. Martiz, M.E. Levenston, P.M. Pinsky, Depth-dependent transverse shear properties of the human corneal stroma, Invest. Ophthalmol. Vis. Sci. 53 (2) (2012) 873–880.
[40] H. Hatami-Marbini, Viscoelastic shear properties of the corneal stroma, J. Biomech. 47 (3) (2014) 723–728.
[41] T.M. Nguyen, J.F. Aubry, D. Touboul, M. Fink, J.L. Gennisson, J. Bercoff, M. Tanter, Monitoring of cornea elastic properties changes during UV-A/riboflavin-induced corneal collagen cross-linking using supersonic shear wave imaging: a pilot study, Invest. Ophthalmol. Vis. Sci. 53 (9) (2012) 5948–5954.
[42] Y. Li, S. Moon, J.J. Chen, Z. Zhu, Z. Chen, Ultrahigh-sensitive optical coherence elastography, Light 9 (2020) 58.
[43] X. Feng, G.Y. Li, S.H. Yun, Ultra-wideband optical coherence elastography from acoustic to ultrasonic frequencies, Nat. Commun. 14 (2023) 4949.
[44] F. Zvietcovich, A. Nair, M. Singh, S.R. Aglyamov, M.D. Twa, K.V. Larin, In vivo assessment of corneal biomechanics under a localized cross-linking treatment using confocal air-coupled optical coherence elastography, Biomedic. Optics Express 13 (5) (2022) 2644–2654.
[45] T. Mekonnen, X. Lin, C. Zevallos-Delgado, M. Singh, S.R. Aglyamov, V. Coulson-Thomas, K.V. Larin, Longitudinal assessment of the effect of alkali burns on corneal biomechanical properties using optical coherence elastography, J. Biophotonics 15 (8) (2022) e202200022.
[46] Z. Jin, R. Khazaeinezhad, J. Zhu, J. Yu, Y. Qu, Y. He, Y. Li, T.E.G. Alvarez-Arenas, F. Lu, Z. Chen, In-vivo 3D corneal elasticity using air-coupled ultrasound optical coherence elastography, Biomedic. Optics Express 10 (12) (2019) 6272–6285.

Supplementary materials

Simultaneous tensile and shear measurement of the human cornea *in vivo* using S0- and A0-wave optical coherence elastography

Guo-Yang Li[1,†,#], Xu Feng[1,†], Seok-Hyun Yun[1,2,*]

[1] Harvard Medical School and Wellman Center for Photomedicine, Massachusetts General Hospital, 50 Blossom St., Boston, MA 02114, USA.

[2] Harvard-MIT Division of Health Sciences and Technology, Cambridge, MA 02139, USA.

[#] Current address: Department of Mechanics and Engineering Science, College of Engineering, Peking University, Beijing 100871, China

[†] Equal contribution

*Correspondence: syun@hms.harvard.edu

Supplementary Note S1. Acoustoelastic model for guided waves in the cornea

The wave equation for small-amplitude plane elastic wave in a prestressed solid [1], is

$$\alpha\frac{\partial^4\psi}{\partial x_1^4}+2\beta\frac{\partial^4\psi}{\partial x_1^2\partial x_2^2}+\gamma\frac{\partial^4\psi}{\partial x_2^4}=\rho\left(\frac{\partial^4\psi}{\partial x_1^2\partial t^2}+\frac{\partial^4\psi}{\partial x_2^2\partial t^2}\right), \tag{S1}$$

where the stream function ψ is related to the displacement components u_1 and u_2 via the relation of $u_1=\psi_{,2}$ and $u_2=-\psi_{,1}$. These relations promise $u_{1,1}+u_{2,2}=0$, which is equivalent to the material incompressible constraint adopted in this study. ρ and t denote the density and time, respectively. The coefficients α, β, and γ are determined by the constitutive law and the stretch ratio λ,

$$\alpha=\mathcal{A}^0_{1212}, 2\beta=\mathcal{A}^0_{1111}+\mathcal{A}^0_{2222}-2\mathcal{A}^0_{1122}-2\mathcal{A}^0_{1221}, \gamma=\mathcal{A}^0_{2121}, \tag{S2}$$

where the fourth-order tensor, A_{0ijkl}, is the Eulerian elasticity tensor and is defined as

$$\mathcal{A}^0_{ijkl}=F_{iI}F_{kJ}\frac{\partial^2 W}{\partial F_{jI}\partial F_{lJ}}, \qquad i,j,k,l,I,J\in\{1,2,3\} \tag{S3}$$

where $\mathbf{F}$ is the deformation gradient tensor and W is the strain energy function. In Eq. (S3) the Einstein summation convention is adopted. For the HGO model, the strain energy is

$$W=\frac{\mu}{2}(I_1-3)+\frac{k_1}{k_2}\sum_{i=1}^{2}\left\{e^{k_2[\kappa(I_1-3)+(1-3\kappa)(I_{4i}-1)]^2}-1\right\}, \tag{S4}$$

where μ, k_1, k_2 and κ are constitutive parameters. μ denotes the initial shear modulus. The dimension of k_1 is the same as μ, whereas k_2 is a dimensionless parameter which determines the nonlinear hardening effect of the collagen fibrils when being stretched. $\kappa=0$ if the collagen fibrils are ideally aligned [2], which is appliable for the cornea. $I_1=\mathrm{tr}(\mathbf{F}^{\mathrm{T}}\mathbf{F})$. I_{41} and I_{42} are two invariants related to two families of collagen fibers. Following the coordinate system (x_1, x_2, x_3) shown in Fig. 1C, the axes of the collagen fibers of the cornea, denoted by unit vectors $\mathbf{M}$ and $\mathbf{M}'$, are aligned with x_1 and x_3, i.e., $\mathbf{M}=(1,0,0)^{\mathrm{T}}$ and $\mathbf{M}'=(0,0,1)^{\mathrm{T}}$. Then I_{41} and I_{42} can be determined [2] by $\mathbf{M}$ and $\mathbf{M}'$:

$$I_{41}=(\mathbf{FM})\cdot(\mathbf{FM}), \quad I_{42}=(\mathbf{FM}')\cdot(\mathbf{FM}'). \tag{S5}$$

With the strain energy function and the deformation tensor, the Cauchy stress tensor can be determined by

$$\sigma_{ij}=F_{iI}\,\partial W/\partial F_{jI}-\bar{p}\delta_{ij}, \tag{S6}$$

where $\bar{p}$ is a Lagrange multiplier for material incompressibility and δ_{ij} is the Kronecker delta.

In this study, we consider a biaxial stretch, $\mathbf{F}=\mathrm{diag}(\lambda,\lambda^{-2},\lambda)$, where λ is the stretch ratio along x_1 (or x_3) axis. With $\sigma_{22}=0$ we can obtain ($\sigma=\sigma_{11}=\sigma_{33}$)

$$\sigma=\mu(\lambda^2-\lambda^{-4})+2k_1\lambda^2(\lambda^2-1)e^{\left[k_2(\lambda^2-1)^2\right]}. \tag{S7}$$

According to the Young-Laplace equation, $\sigma=\mathrm{IOP}\times R/(2h)$. Therefore, the stretch ratio λ can be obtained by solving the nonlinear equation

$$\mu(\lambda^2-\lambda^{-4})+2k_1\lambda^2(\lambda^2-1)e^{\left[k_2(\lambda^2-1)^2\right]}=\mathrm{IOP}\times R/(2h). \tag{S8}$$

The coefficients α, β, and γ can be obtained by inserting Eqs. (S3) and (S4) into Eq. (S2),

$$\begin{gathered}\alpha=\lambda^2\left\{\mu+2k_1(\lambda^2-1)e^{\left[k_2(\lambda^2-1)^2\right]}\right\},\qquad \gamma=\mu\lambda^{-4}.\\ 2\beta=\alpha+\gamma+4k_1\lambda^4[2k_2(\lambda^2-1)^2+1]e^{\left[k_2(\lambda^2-1)^2\right]},\end{gathered} \tag{S9}$$

In the absence of prestress (i.e., $\lambda=1$)

$$\alpha=\mu,\quad \beta=\mu+2k_1,\quad \gamma=\mu. \tag{S10}$$

Next, we consider the guided wave motion in the cornea. It should be noted the boundary conditions (BCs) have pronounced effects on the dispersion relations of the guided waves. The two sides of the cornea are air and aqueous humor. In our simplified model (see Fig. 1C), the aqueous humor is modeled as a semi-infinite fluid layer and the wave equation is

$$\nabla^2\chi=\frac{\rho^f}{\nu}\chi_{,tt}, \tag{S11}$$

where ν (2.2 GPa) and ρ^f (1,000 kg/m^3) denote the bulk modulus and density of the fluid, respectively. The potential function χ is related to the displacement of the fluid (denoted by $\mathbf{u}^f$) via the relations of $u_1^f=\chi_{,1}$ and $u_2^f=\chi_{,2}$. The pressure of the fluid, denoted by p^*, is determined by

$$p^*=-\nu\nabla\cdot\mathbf{u}^f. \tag{S12}$$

At the liquid-tissue interface ($x_2=0$), the following boundary conditions are applied:

$$\begin{gathered}u_2=u_2^f,\quad -\gamma\psi_{,11}+\gamma\psi_{,22}=0,\quad \rho\psi_{,2tt}-(2\beta+\gamma)\psi_{,112}-\\ \gamma\psi_{,222}=-p_{,1}^*.\end{gathered} \tag{S13}$$

At $x_2=h$, the boundary is stress free, which gives

$$-\gamma\psi_{,11}+\gamma\psi_{,22}=0,\quad \rho\psi_{,2tt}-(2\beta+\gamma)\psi_{,112}-\gamma\psi_{,222}=0. \tag{S14}$$

More details on the derivations of the boundary conditions can be found in Refs. [3] and [4].

We seek the plane wave solutions for $\psi(x_1,x_2,t)$ and $\chi(x_1,x_2,t)$, i.e.,

$$\begin{cases}\chi(x_1,x_2,t)=\chi_0(x_2)e^{\iota k(x_1-ct)}\\ \psi(x_1,x_2,t)=\psi_0(x_2)e^{\iota k(x_1-ct)},\end{cases} \tag{S15}$$

where $\iota=\sqrt{-1}$, k is the wavenumber, and c is the phase velocity. Inserting Eq. (S15) into Eqs. (S1) and (S11), we can get

$$\begin{cases}\chi=Ae^{-\xi kx_2}e^{\iota k(x_1-ct)}\\ \psi=[B_1\cosh(s_1kx_2)+B_2\sinh(s_1kx_2)+B_3\cosh(s_2kx_2)+B_4\sinh(s_2kx_2)]e^{\iota k(x_1-ct)}\end{cases} \tag{S16}$$

The parameters s_1, s_2 and ξ are determined by

$$\gamma s^4 - (2\beta - \rho c^2)s^2 + (\alpha - \rho c^2) = 0, \tag{S17}$$

and

$$\xi^2 - 1 = -c^2\rho^f/\nu. \tag{S18}$$

Substituting $\psi(x_1, x_2, t)$ and $\chi(x_1, x_2, t)$ in Eqs. (S13) and (S14), we get

$$M_{5\times5} \cdot [B_1, B_2, B_3, B_4, A]^{\mathrm{T}} = 0. \tag{S19}$$

The nonzero components of $\mathbf{M}$ are

$$\begin{gathered}
M_{11} = s_1^2 + 1, M_{13} = s_2^2 + 1, \\
M_{22} = \gamma s_1(s_2^2 + 1), M_{24} = \gamma s_2(s_1^2 + 1), M_{25} = \iota\rho^f c^2, \\
M_{31} = 1, M_{33} = 1, M_{35} = -\iota\xi, \\
M_{41} = (s_1^2 + 1)\cosh(s_1 kh), M_{42} = (s_1^2 + 1)\sinh(s_1 kh), \\
M_{43} = (s_2^2 + 1)\cosh(s_2 kh), M_{44} = (s_2^2 + 1)\sinh(s_2 kh), \\
M_{51} = s_1(s_2^2 + 1)\sinh(s_1 kh), M_{52} = s_1(s_2^2 + 1)\cosh(s_1 kh), \\
M_{53} = s_2(s_1^2 + 1)\sinh(s_2 kh), M_{54} = s_2(s_1^2 + 1)\cosh(s_1 kh).
\end{gathered} \tag{S20}$$

In this derivation, we have used the identity

$$2\beta - \rho c^2 = \gamma(s_1^2 + s_2^2), \tag{S21}$$

which is obtained from Eq. (S17). The existence of nontrivial solution to Eq. (S19) requires

$$\det(\mathbf{M}_{5\times5}) = 0. \tag{S22}$$

This is the secular equation for the guided waves in the cornea.

Reference

1. M. Destrade and G. Saccomandi, Waves in nonlinear pre-stressed materials. *Springer Science & Business Media.* **495**, 1–26 (2007).

2. T. C. Gasser, R. W. Ogden, G. A. Holzapfel, Hyperelastic modelling of arterial layers with distributed collagen fibre orientations. *J. R. Soc. Interface*. **3**, 15–35 (2005).

3. G.-Y. Li, Q. He, R. Mangan, G. Xu, C. Mo, J. Luo, M. Destrade, Y. Cao, Guided waves in pre-stressed hyperelastic plates and tubes: Application to the ultrasound elastography of thin-walled soft materials. *J. Mech. Phys. Solids*. **102** (2017).

4. M. Otténio, M. Destrade, R. W. Ogden, Acoustic waves at the interface of a pre-stressed incompressible elastic solid and a viscous fluid. *Int. J. Non. Linear. Mech.* **42**, 310–320 (2007).

Supplementary Note 2. Phase velocities of the A_0 and S_0 modes at the high and low frequency limits

If the wave frequency approaches to the infinity and the material properties are invariant over frequency, the dispersion relations of A0 and S0 exhibit plateaus (Fig. S2A). Let us denote the high frequency-limit phase velocities as c_∞^{A0} and c_∞^{S0}, respectively. c_∞^{A0} is equivalent to the speed of the interfacial wave at the fluid-cornea interface (i.e., Scholte wave). c_∞^{S0} is equivalent to the speed of the surface wave at the free surface of the cornea (i.e., Rayleigh wave). $c_S = \sqrt{\alpha/\rho}$ is the bulk shear wave speed along the x_1 axis.

In the absence of prestress (i.e., $\lambda = 1$), $c_{\mathrm{S}} = \sqrt{\mu/\rho}$. The dependences of $c_\infty^{\mathrm{A0}}/c_S$ and $c_\infty^{\mathrm{S0}}/c_S$ on an anisotropy parameter $2k_1/\mu$ are shown in Fig. S2B. $c_\infty^{\mathrm{A0}}/c_S$ and $c_\infty^{\mathrm{S0}}/c_S$ increase slightly with $2k_1/\mu$ but are always slightly smaller than 1. For isotropic material ($k_1 = 0$), we have $c_\infty^{\mathrm{A0}}/c_S \approx 0.839$, $c_\infty^{\mathrm{S0}}/c_S \approx 0.955$. For highly anisotropic material ($2k_1/\mu \gg 1$), c_∞^{A0} and c_∞^{S0} become closer to the bulk shear wave speed c_S. Therefore, the measurement of c_∞^{A0} and c_∞^{S0} can give a good estimate of the shear modulus μ.

The phase velocity of S0 at near-zero frequency is nonzero and denoted as c_0^{S0}. It can be shown that $c_0^{\mathrm{S0}} = \sqrt{(2\beta + 2\gamma)/\rho}$. In the absence of prestress (Eq. (S10)), we find $c_0^{\mathrm{S0}} = 2\sqrt{(\mu + k_1)/\rho}$. From c_0^{S0}, the anisotropic material parameter k_1 can be determined. c_0^{S0} is also directly related to the plane-strain Young's modulus along the x_1 axis. The plane strain modulus is the ratio between the uniaxial stress and strain when the material is stretched along the x_1 axis while it is constrained in the orthogonal direction along the x_3 axis. The plane-strain modulus $E_{xx}^{\sigma=0}$ is equal to $4\mu + 4k_1$. For isotropic materials, represented by $k_1 = 0$, $E_{xx}^{\sigma=0} = 4\mu$. This relationship is known for incompressible materials with a Poisson's ratio of 0.5.

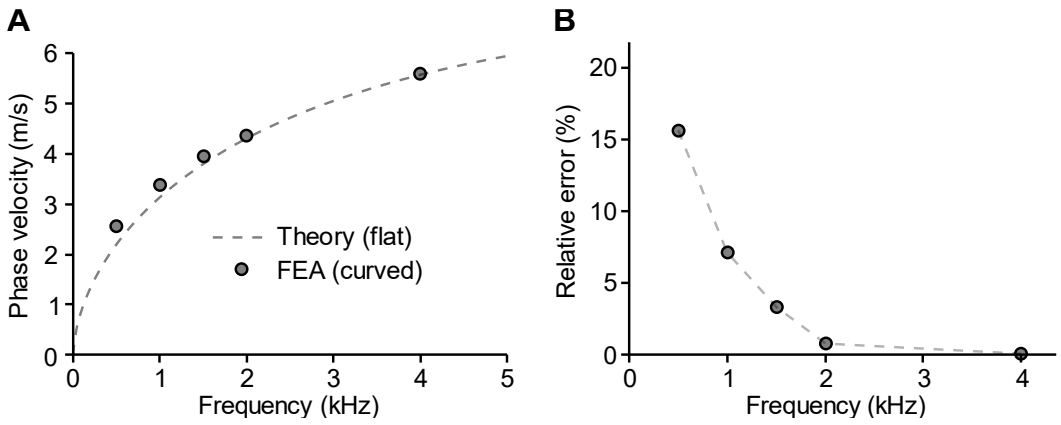

Fig. S1: Influence of corneal curvature on wave speed. (A) Phase velocity dispersion relation. Dashed line: theoretical model assuming the cornea is flat. Circles: Finite element analysis (FEA) simulation considering corneal curvature. (B) Relative error of the phase velocities between the theory for the flat cornea and the FEA simulation of the curved cornea. The relative error becomes negligible at 4 kHz, as the wavelength is significantly smaller than the radius of curvature.

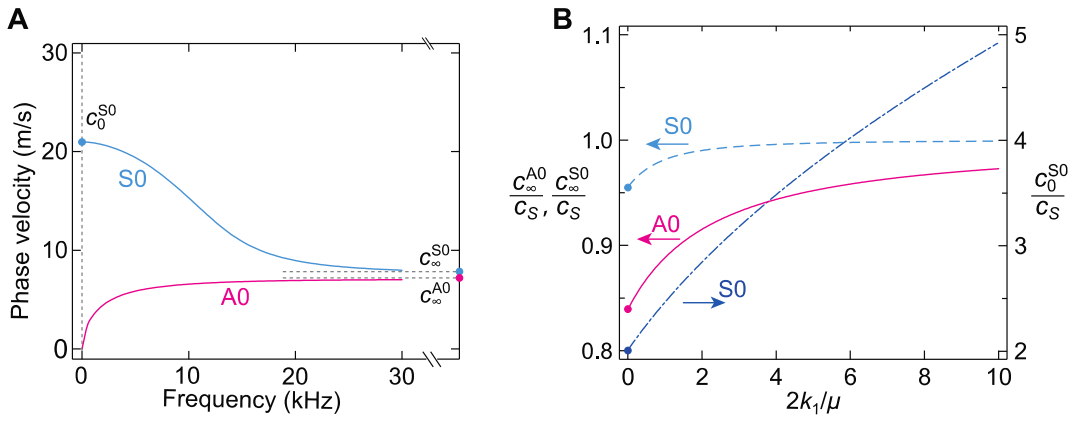

Fig. S2: (A) Phase velocities of A0 and S0 waves over frequency. c_∞^{A0} and c_∞^{S0} denote the phase velocities of the A0 and S0 waves at infinite frequency. c_0^{S0}, phase velocity of the S0 at zero frequency. (B) Dependences of c_∞^{A0}, c_∞^{S0}, and c_0^{S0} on the material anisotropy. For isotropic materials ($2k_1/\mu = 0$), we obtain $c_\infty^{\mathrm{A0}}/c_S \approx 0.839$ (the Scholte wave speed), $c_\infty^{\mathrm{S0}}/c_S \approx 0.955$ (the Rayleigh wave speed), and $c_0^{\mathrm{S0}}/c_T = 2$.

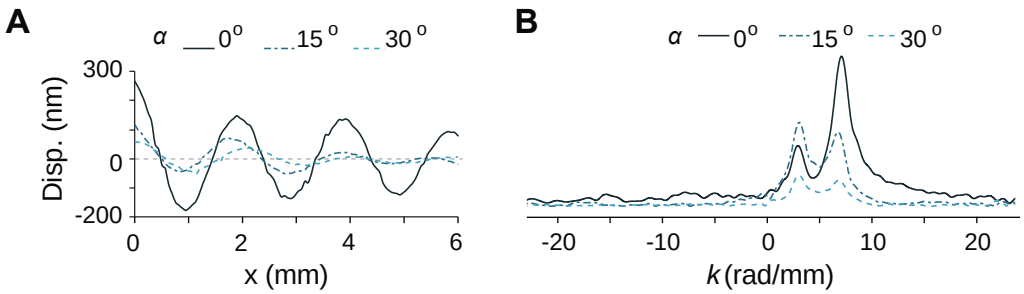

Fig. S3: Optimization of the probe tip angle α. (A) Total displacement amplitude at 4 kHz at different angles. (B) Wavenumber domain plot showing the amplitude ratio of the S0 and A0 waves at 12 kHz.

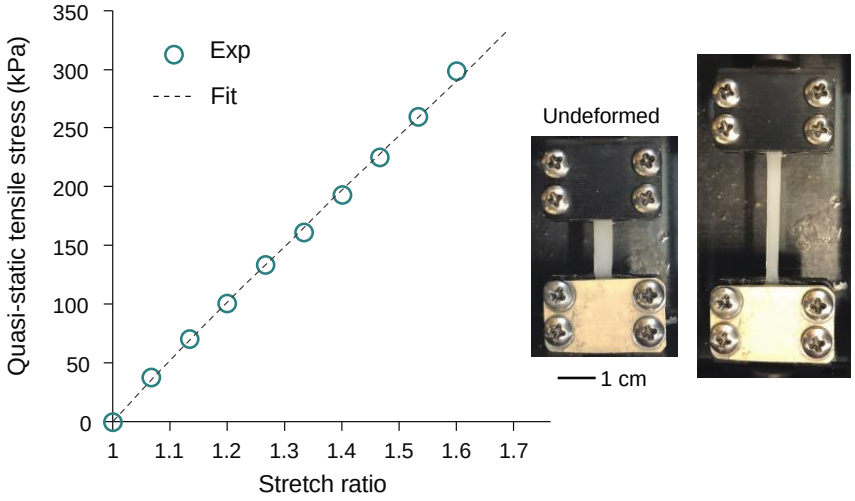

Fig. S4: Tensile test of the rubber phantom using (eXpert 4000 Micro Tester, Admet, Norwood, USA). A small piece of 5 mm × 18 mm × 0.45 mm was cut for the test. The initial shear modulus $\mu =$ 180 kPa is obtained by curve fitting the stress-strain curve. Inset, a sample at the undeformed and deformed states, respectively.

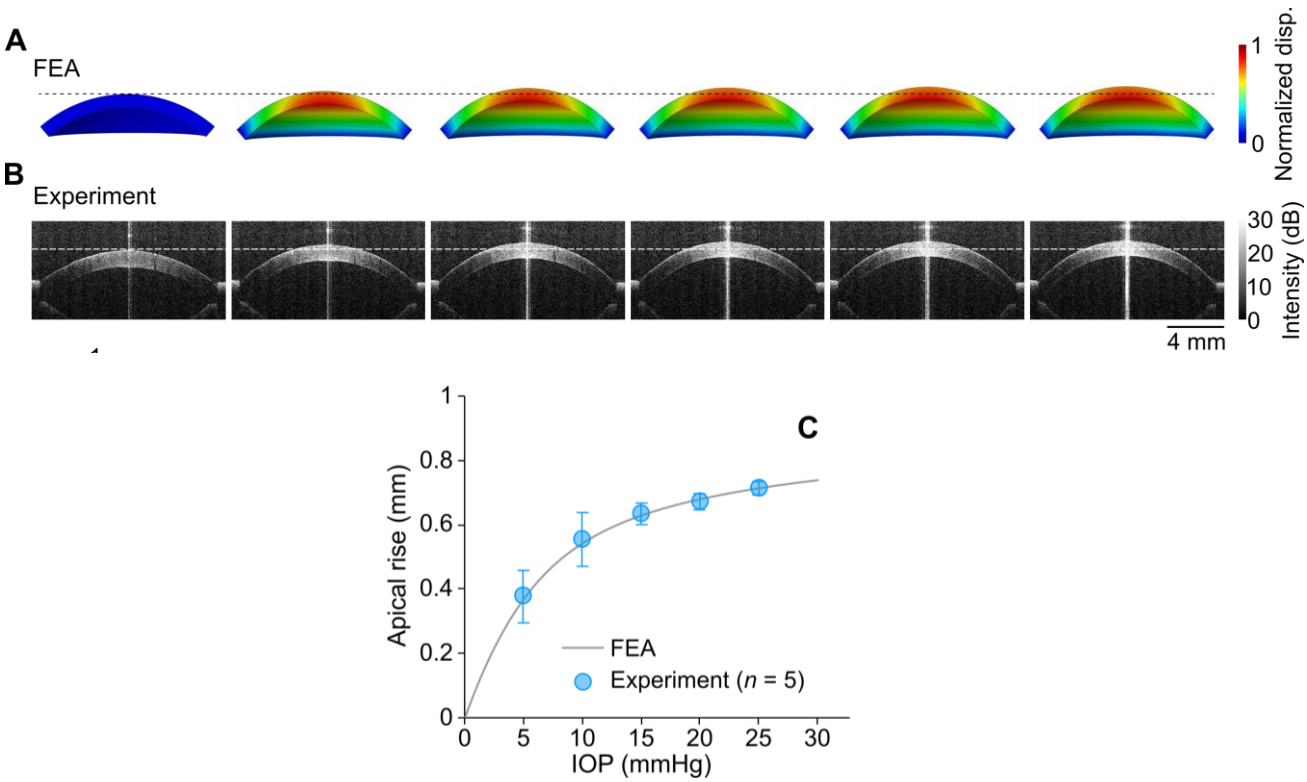

Fig. S5: Inflation test of the porcine cornea. (A) FEA to show deformation of the cornea. (B) OCT images of the inflated corneas as the intraocular pressure is increased. From left to right, IOP = 0, 5, 10, 15, 20, and 25 mmHg. (C) Comparison of the apical rise between FEA and experiment (5 measurements at each IOP level).